RSC Advances

RSC Advances

ARTICLE

Preparation and catalytic performance of a novel highly dispersed bifunctional catalyst Pt@Fe-MCM-41

Naijin Wu, Baoshan Li*, Jianjun Liu, Shengli Zuo, Yunchen Zhao

A novel highly dispersed bifunctional catalyst Pt@Fe-MCM-41 was prepared successfully by in situ synthesis combined with selective reduction. The catalyst contains highly dispersed metal active components and acid carrier with regular structure. The results showed that the platinum nanoparticles with uniform size were highly dispersed and fixed in the inner surface of MCM-41 and the iron atoms were tetrahedral coordinated and highly dispersed in the silica framework. The samples showed an excellent catalytic activity and selectivity for hydrocracking of residual oil, which proved that there existed an obvious promotion effect between the highly dispersed platinum active sites and the Fe-MCM-41 carrier.

1. Introduction

Secondary processing in the field of petroleum chemical industry needs a kind of important catalytic materials, namely the hydrocracking catalyst. This type of catalyst belongs to a bifunctional material[1], which is not only contains metal active sites possessing hydrogenation–dehydrogenation function, but also contains a large number of acidic centres from the carrier for the cracking of macromolecular hydrocarbons.[2-8] Zeolite molecular sieves with narrow and uniform pore size distribution and more acidic centres are often used as the carrier of bifunctional catalyst[9], but the smaller pore size limits the diffusion of large molecules, especially in the process of hydrogenation cracking and reforming.[10-14] Until the synthesis of mesoporous molecular sieves in 1992, it opened a new area for the solution of the aperture problem.[15-16] However, the number of acidic centres provided by the pure silica mesoporous molecular sieves is fewer and the hydrothermal stability is poor, which limit its application in catalysis field. In order to overcome these defects, many scientific research has been devoted to the modification or functionalization of silica mesoporous materials, such as doping or loading high active metal components.[17-19] From the literature[20], it can be seen that introducing heteroatoms into the siliceous framework could enhance the hydrothermal stability and increase the acid sites of this materials. And loading metal components can also increase the metal active sites in heterogeneous catalysis. Qin[21] et al. synthesised well-ordered Ni-MCM-41 with high

nickel content and this material exhibited an excellent catalytic performance for the hydrocracking of coker wax oil. Alsobaai et al. prepared a series of NiW/MCM-48 catalysts modified with Al using the incipient wetness method, and the good catalytic activity for hydrocracking of petroleum gas oil was improved with increasing metal content.[22] Seo et al. synthesized a catalyst Pt-loaded mesoporous aluminosilicate (Pt/Al-SBA-15) for the hydrocracking of Fischer-Tropsch waxes.[23] And the catalytic activity of Pt/Al-SBA-15 was stronger than a Pt-loaded microporous zeolite (Pt/β-zeolite). Barrón C. et al. prepared many heterogeneous catalysts (Ni-Mo, Ni-W carbides, Pt and triflic acid) supported on mesoporous SBA-15.[24] The catalytic results of selective hydrocracking of long hydrocarbons chains indicate the strong influence of the surface acidic active sites. Li et al. introduced numerous transition metal into the molecular sieve framework and prepared a modified micro/mesoporous composite materials, the material has very high catalytic activity for hydrocracking of coke gas oil.[25]

In order to improve the utilization of metal component and reduce the catalyst cost, more and more research were focused on how to improve the dispersion of metal active sites. On the basis of solving this problem, if a good combination of the highly dispersed metal active sites and highly dispersed acid sites can be achieved, it will be greatly improved the catalytic activity of the modified mesoporous materials for the hydrogenation of large molecules.

In this paper, a new type of highly dispersed bifunctional catalyst Pt@Fe-MCM-41 was successfully prepared by in situ synthesis and selective reduction. First, the metal components were fixed into the framework via hydrothermal crystallization, and then only the platinum atoms were reduced under appropriate temperature. In this catalyst, Fe irons were highly dispersed in the framework of MCM-41 with

State Key Laboratory of Chemical Resource Engineering, Beijing University of Chemical Technology, No. 15 Beisanhuan East Road, Beijing 100029, P. R. China. E-mail: bsli@mail.buct.edu.cn; Fax: +86-010-64445611; Tel: +86-010-64445611
Electronic Supplementary Information (ESI) available: [details of any supplementary information available should be included here]. See DOI: 10.1039/x0xx00000x

isomorphous substitution and platinum nanoparticles were highly dispersed in the inner surface of the mesoporous channels, so that the catalyst has the highly dispersed acid and metal active sites simultaneously.

2. Experimental

2.1 Preparation of the sample Pt@Fe-MCM-41

The procedure detail was conducted as follows: 3.6 g of CTAB was dissolved in 70 mL of deionized water in a three-necked flask with vigorous stirring until obtain a clear solution. Take a certain amount of ferric nitrate into a beaker and the well-prepared tartaric acid solution (1mol/L) was added into the beaker continuingly with a fully stirring to form a stable ligand solution, the molar ratio of ferric nitrate and tartaric acid was 1:1. And then the uniform ligand solution was added into the flask with a strong stirring for 1 h and form a viscous solution. In addition, 0.02 g of K_2PtCl_6 was dissolved in a beaker and added dropwise to the obtained solution with continuous stirring until a uniformly sol was formed. The molar composition of the mixture except the metal components was $1.0TEOS:0.22CTAB:0.56NaOH:115H_2O$. Then, the mixture was transferred into a static Teflon-lined stainless steel autoclave and heated under autogenous pressure at 110 ^{o}C for 96 h. After crystallization, the product was washed with distilled water until the pH value is neutral, and dried at 110 ^{o}C to get the as-synthesized samples for the next procedure.

0.3-0.5 g of dried sample was positioned in the bottom of a quartz tube and heated in hydrogen from room temperature to 400 ^{o}C at a rate of 5 ^{o}C /min and kept 400 ^{o}C for 120 min to make sure that platinum components was fully reduced. It was then allowed to cool naturally to room temperature and calcined at 400 ^{o}C in air for 5 h to remove the residual surfactant in muffle furnace. The resulting sample was designated as 0.3%Pt@*x*%Fe-MCM-41 (here *x*% is weight percentage of Fe).

2.2 Synthesis of contrast sample

The preparation of pure Si-MCM-41 was identical with the above conditions except for the addition of metal, the crystallized sample was dried and calcined at 550 ^{o}C for 6 h. The compared sample 12%Fe/MCM-41-TM was prepared by traditional impregnation (TM) method. The specific procedure is: the pure Si-MCM-41 samples were immersed in ferric nitrate solution and heated with a uniform magnetic stirring, until the solution evaporated completely. The dried samples were calcined at 550 ^{o}C for 6 h. Additionally, Si-MCM-41 was dipped in ferric nitrate and K_2PtCl_6 solution in turn and 0.3%Pt-12%Fe/MCM-41-TM sample was prepared by the same TM method. The compared sample 12%Fe-MCM-41 was prepared by hydrothermal crystallization, the synthesis procedure was same as the Pt@Fe-MCM-41 synthetic methods except for the platinum addition and the removal of template was achieved by calcined at 550 ^{o}C for 6 h in air. Then, the 12%Fe-MCM-41 sample was impregnated with 0.3% Pt via TM method and the result sample was named as 0.3%Pt/12%Fe-MCM-41.

2.3 Characterization

The metal content was measured by the inductively coupled plasma atomic emission spectrometry (ICP-AES) on the ICPS-7500 plasma emission spectrometer. The X-ray powder diffraction (XRD) patterns were tested with a Rigaku UItimaIII diffractometer using Cu-Kα radiation (λ= 0.1541 nm) in low-angle range ($2\theta = 0.5\text{-}8^{°}$) and wide-angle range ($2\theta = 5^{°}\text{-}70^{°}$). The pore morphology of the samples, the sizes and the distribution of the platinum particles in the samples were examined by high-resolution transmission electron microscopy (HRTEM) on a JEM-2100 microscope with an accelerating voltage of 200 kV. Before examination, the samples were dispersed by using absolute alcohol in ultrasonic dispersion. The element distribution maps were obtained using a Hitachi S-4700 scanning electron microscope (SEM). The nitrogen adsorption–desorption isotherms were determined on Quandasorb SI four station automatic surface and pore size analyzer at the liquid nitrogen temperature. Before testing, samples were degassed at 200 ^{o}C for 6 h in a vacuum. The pore size distribution curves were calculated from the desorption branch of the isotherm. The UV–vis diffuse reflectance spectra were measured with a Shimadzu UV–3600 UV-VIS-NIR spectrophotometer using $BaSO_4$ as the background standard. The X-ray photoelectron spectroscopy (XPS) analyses were obtained on an ESCALAB 250Xi spectrometer equipped with an Al Kα X-ray source from Thermo Fisher Company. The reduction temperature of the metal in the samples were tested by hydrogen temperature programmed reduction (H_2-TPR) on ChemiSorb 2720 chemical adsorption apparatus.

2.4 Catalytic performance test

The catalyst activity was investigated by hydrocracking reaction of residual oil. Specific operation process is as follows: 0.1 g of catalysts and quartz sand were mixed evenly and then placed into fixed bed reactor (H200mm×Φ10mm). When the reactor was heated to a specified temperature, the liquid residue oil after preheated was pumped using TBP1010 type medium pressure constant flow pump. The range of weight hourly space velocity (WHSV) was 6-12 h^{-1}. During the whole procedure, the mass ratio of residue oil and catalyst was about 100:1 and the system pressure was maintained constant by using a counterbalance valve. The gas and liquid products were collected using gas collecting bag and conical flask, respectively. After subsection distillation of liquid products, according to the classification of petroleum products, the low temperature fraction of 70-120 ^{o}C was defined as gasoline, and the fraction of 120-160 ^{o}C was defined as kerosene. To calculate coke yield, the catalyst residue was dissolved completely with hydrofluoric acid at room temperature, and then the liquid acid was neutralized by adding $NaHCO_3$. The final mixture were filtered, washed, dried and weighed to calculate the amount of coke. In addition, the liquid residue after the distillation was also washed with acetone to be counted in the total coke yield.

3. Results and discussion

ARTICLE

Table 1 Structure properties of the 0.3%Pt@x%Fe-MCM-41 and Si-MCM-41 samples

sample	Pt (wt%)	Fe (wt%)	S_{BET} (m^2/g)	unit cell parameter [a] (Å)	pore diameter (Å)	pore volume (cm^3/g)	wall thickness (Å)
Si-MCM-41	—	—	1192	38.9	22.9	1.13	16.0
0.3%Pt@7%Fe-MCM-41	0.26	6.36	997	41.7	25.6	1.23	16.1
0.3%Pt@10%Fe-MCM-41	0.23	8.98	878	42.4	25.7	1.26	16.7
0.3%Pt@12%Fe-MCM-41	0.25	11.3	832	43.6	25.9	1.28	17.7

[a] Unit cell parameter = 2 × d100/(3)$^{1/2}$ (from XRD).

3.1 Characterization

In the three highly dispersed bifunctional samples, the content of platinum is 0.3 wt% and the theoretical content of iron is 7wt%, 10wt% and 12wt%, respectively. The three samples are named 0.3%Pt@7%Fe-MCM-41, 0.3%Pt@10%Fe-MCM-41 and 0.3%Pt@12%Fe-MCM-41, respectively. The actual metal content from ICP test was listed in Table 1. It can be seen that the actual measured metal content in each sample is slightly lower than the theoretical value, but the difference is within the operation error, which prove that almost of the metal components are introduced into the samples using this method.

Fig. 1A represents the low-angle XRD diffraction spectrum of different samples. It can be seen that all the samples showed three obvious peaks corresponding to the characteristics diffraction of MCM-41, indicating that all of the samples have a regular mesoporous structure. For the 0.3%Pt@x%Fe-MCM-41 samples, the diffraction peak is shifted to the small angle in turn with the increase of the iron content. It illustrates that the interplanar spacing d and lattice parameter a_0 are gradually increased, which is calculated by the Bragg equation $2d\sin\vartheta$=n•λ and the equation of a_0 = 2×d100/(3)$^{1/2}$, respectively. And all of the d and a_0 values are larger than that of pure Si-MCM-41. The most likely reason may be that the larger metal heteroatoms substituted the small silicon atom and were incorporated into the MCM-41 framework successfully, which leads to the increase of pore size and pore wall thickness. In addition, there is a little reduction and broadening of the diffraction peaks when the metal content increasing, indicating a slight reduction in hexagonal mesoporous structure.

Fig. 1B represents the wide-angle XRD patterns of the samples. The curves of all the 0.3%Pt@x%Fe-MCM-41 samples are almost the same with Si-MCM-41 without any characteristic diffraction peaks of metal or metal oxides. It proves that the platinum nanoparticles did not form a large crystal and highly dispersed in the interior of pore structure. In addition, the iron atoms may be incorporated into the framework of MCM-41 completely, which corresponding to the low-angle XRD result.

The HRTEM pictures of all the bifunctional samples are shown in Fig. 2 and the size distribution of platinum nanoparticles is list on the right side of the picture (measured from at least 200 particles). It can be seen that all the samples possess a good mesoporous structure, while the small platinum nanoparticles are highly dispersed in an ordered distribution in the inner surface of carrier. Along with the metal content increased, the mean size of the platinum nanoparticles is 2.22 nm, 2.40 nm and 2.43 nm,

respectively. All of them are less than the pore size of molecular sieve listed in table 1. In addition, there is no large metal oxide particles appeared on both of the internal and external carrier surfaces, which further proves that the most of iron atoms are incorporated into the molecular sieve skeleton.

Fig. 3 shows the elements distribution maps of Si, O and Fe. The distribution of each element is very uniform, and is consistent with the shape of the sample. Combined with the above test results, the iron atoms is most likely highly dispersed in the matrix of MCM-41 skeleton.
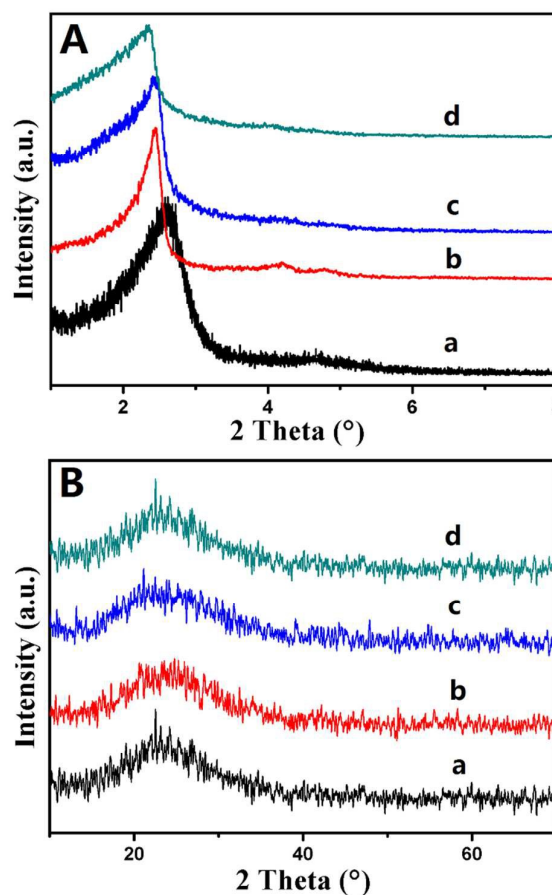
Fig. 1 XRD patterns of all the samples: A-low angle patterns, B-wide angle patterns: a. Si-MCM-41, b. 0.3%Pt@7%Fe-MCM-41, c. 0.3%Pt@10%Fe-MCM-41, d. 0.3%Pt@12%Fe-MCM-41.
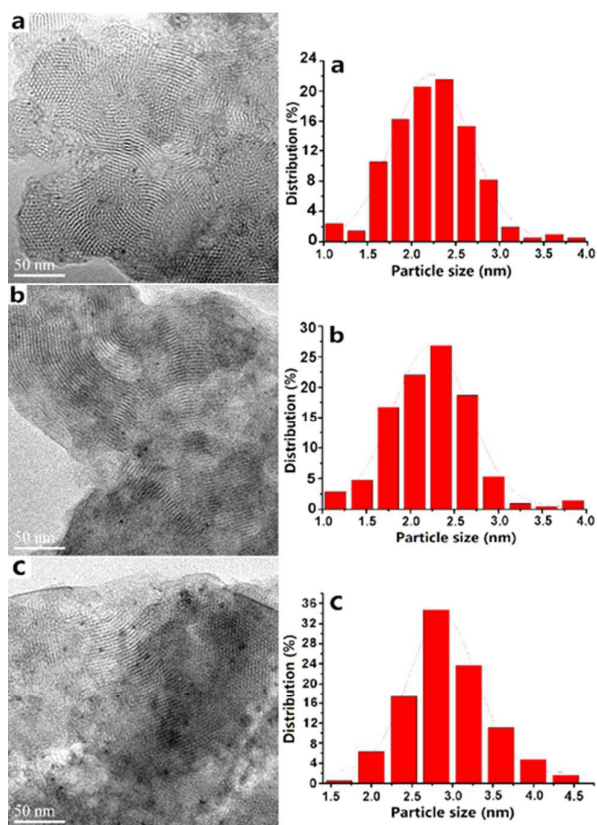
Fig. 2 HRTEM images of the samples and the corresponding Pt particle size distribution: a. 0.3%Pt@7%Fe-MCM-41, b. 0.3%Pt@10%Fe-MCM-41, c. 0.3%Pt@12%Fe-MCM-41.
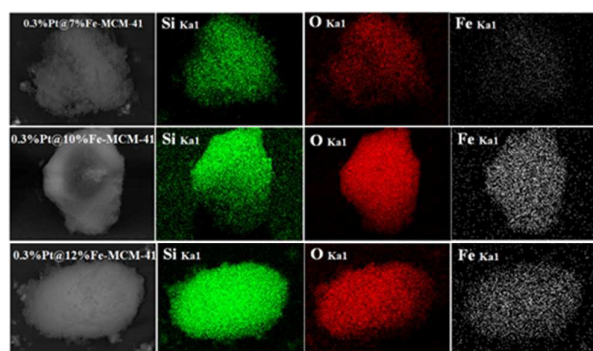
Fig. 3 SEM-mapping images of the bifunctional catalyst samples.

Fig. 4 shows the N_2 adsorption–desorption isotherms (Fig. 4A) and the pore size distribution curves (Fig. 4B) of the 0.3%Pt@x%Fe-MCM-41 samples, and the specific values are given in Table 1. All of the isotherms possess an obvious hysteresis loops, which belong to the typical type IV curve. At the relative pressure of 0.3-0.5, there is an obvious sudden jump, which is caused by the capillary coagulation of nitrogen. This is produced by the typical mesoporous materials. The above phenomenon prove that the samples have a regular mesoporous structure. Fig. 4B Indicates that all the samples have a narrow and uniform pore size distribution, the related

value of cell parameters, pore size and pore volume are listed in table 1. It can be seen that the highest metal content sample 0.3%Pt@12%Fe-MCM-41 also has a large specific surface area of 832 $m^2 \cdot g^{-1}$. Compared with Si-MCM-41, the unit cell parameters, pore size and pore volume of the 0.3%Pt@x%Fe-MCM-41 samples are significantly increased along with the increase of metal content, which may be enlarged by the incorporation of larger metal cations. It confirms that the metal heteroatoms are involved in the formation of the mesoporous pore structure and incorporated into the framework of MCM-41. However, with the increase of the metal content, the specific surface area of bifunctional samples decreased in turn, which may be caused by two kinds of reasons. One is that the weights of metal heteroatoms are larger than that of silicon atom, its incorporation will lead to the relative decrease of surface area in unit mass sample. The other is the incorporation of heteroatom will slightly destroy the regularity of mesoporous structure, consisted with the XRD results.

The UV-vis spectra are shown in Fig.5. For Si-MCM-41 sample, there is no absorption peak in the UV-visible region.
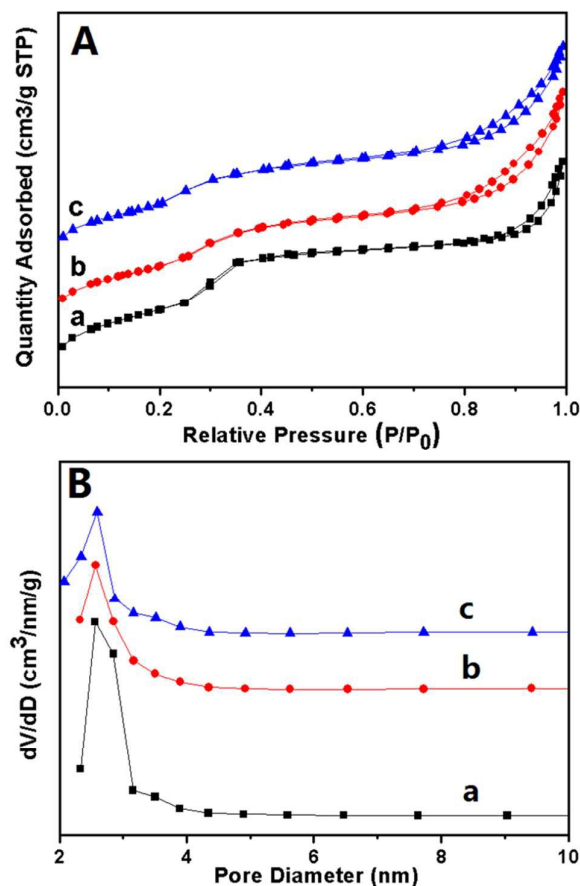
Fig. 4 N_2 adsorption/desorption isotherms (A) and pore size distribution curves (B) of different samples: a. 0.3%Pt@7%Fe-MCM-41, b. 0.3%Pt@10%Fe-MCM-41, c. 0.3%Pt@12%Fe-MCM-41.
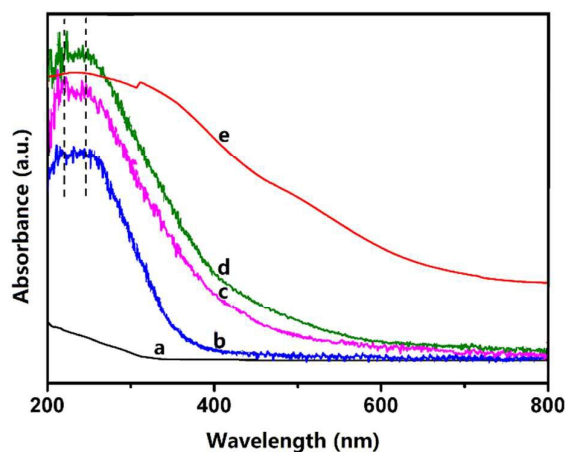
Fig. 5 UV–vis spectra of different samples: a. Si-MCM-41, b. 0.3%Pt@7%Fe-MCM-41, c. 0.3%Pt@10%Fe-MCM-41, d. 0.3%Pt@12%Fe-MCM-41, e. 12%Fe/MCM-41-TM.

On the contrary, there have two obvious absorption peaks appearing at 218 nm and 251 nm in 0.3%Pt@*x*%Fe-MCM-41 samples, which may be caused by the low-energy charge-transfer transitions of $Fe^{3+} \rightarrow O^{2-}$ (tetrahedron lattice).[26-27] This absorption band proves that Fe^{3+} has been introduced into the framework of the molecular sieve and highly dispersed in tetrahedral coordination in the MCM-41 skeleton. Moreover, the radius ratio of Fe/O^{2-} is in the range of 0.214-0.4. According to Pauling rule, Fe^{3+} prefers tetrahedral coordination, which conforming the above results.[28] However, for 12%Fe/MCM-41-TM sample prepared by traditional method, a broad absorption band in 200-700 nm appeared and the strongest absorption peaks are located at the 350 nm and 510 nm, representing the extra framework iron species and the iron oxide clusters or aggregates, respectively.[29-31] The two obvious peaks are attributed to the electronic transition of Fe-O-Fe. In 0.3%Pt@x%Fe-MCM-41 samples, there have no absorption peaks in 350-700 nm, which confirms that most of the iron atoms in bifunctional catalysts were highly dispersed into the framework of MCM-41.

Fig.6 gives the H_2-TPR spectra of different samples and displays the reduction temperature of all metal species. The 12%Fe/MCM-41-TM sample has a strong hydrogen signal peak at 372 °C, which represents the reduction temperature of FeOx species.[32] For the 0.3%Pt@7%Fe-MCM-41 and 0.3%Pt@10%Fe-MCM-41 samples, there only has an obvious signal peak at 775, 658 °C respectively in high temperature region, which demonstrates that the iron species in the two samples are more difficult to be reduced than the FeOx species. The primary reason may be that the most of the iron atoms were introduced into the skeleton of MCM-41 successfully and format a high stability Si-O-Fe bond,[33] corresponding to the above test. At the same time, the reduction temperature of iron has been significantly dropped with the increase of the metal content. This is because the excessive heteroatoms doped will result in a certain destruction of ordered structure, which further decrease the stability of Si-O-Fe framework and lead to the iron species

more easily to be reduced. However, the sample 0.3%Pt@12%Fe-MCM-41 has two hydrogen consumption peaks: a strong one in the high temperature region at 642 °C, a weak one at 396 °C, which illustrate that the
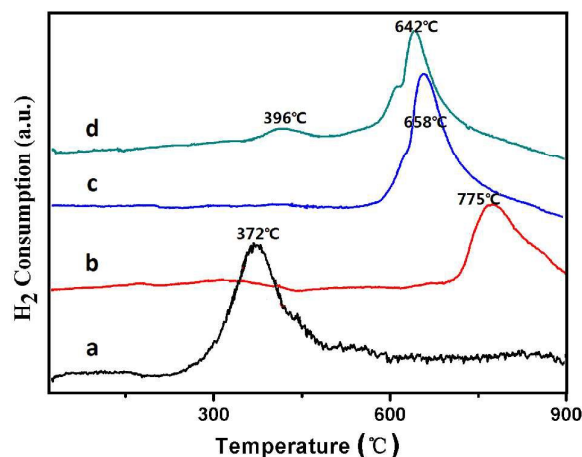
Fig. 6 H_2-TPR spectra of different samples: a. 12%Fe/MCM-41-TM, b. 0.3%Pt@7%Fe-MCM-41, c. 0.3%Pt@10%Fe-MCM-41, d. 0.3%Pt@12%Fe-MCM-41.
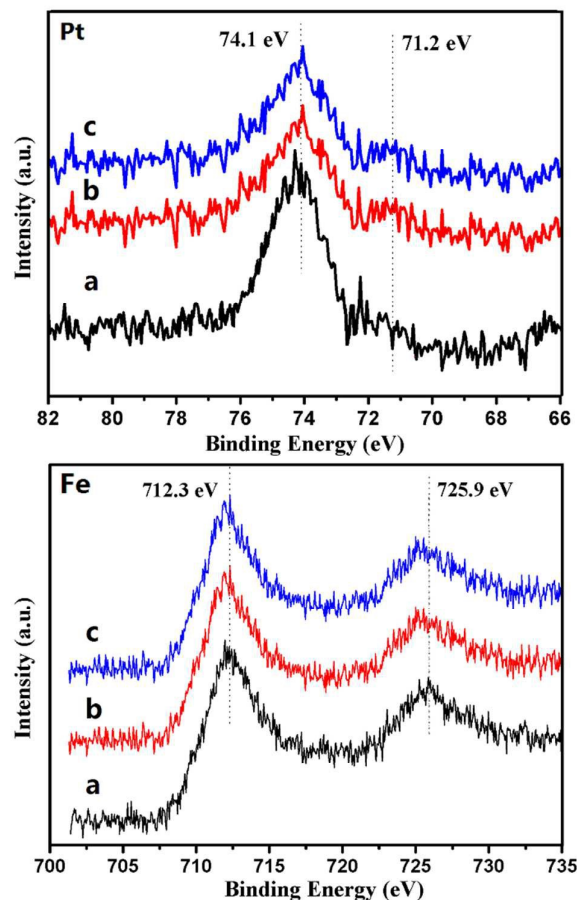
Fig. 7 XPS spectrum of the sample: a. 0.3%Pt@7%Fe-MCM-41, b. 0.3%Pt@10%Fe-MCM-41, c. 0.3%Pt@12%Fe-MCM-41.

highest metal content sample has a very little amount of iron oxide species after calcined. It suggest that the framework metal heteroatom content has a maximum limit. Furthermore, all the 0.3%Pt@x%Fe-MCM-41 samples do not appear any hydrogen consumption peak at about 100-200 °C, which represent the reduction temperature of platinum oxide.[34] It can be obtained that the platinum species have been completely reduced in all bifunctional catalysts.

The XPS spectra of the bimetallic samples are depicted in Fig. 7. For all the samples, there are two obvious characteristic peak at 71.2 eV and 74.1 eV, on behalf of the binding energy of Pt4f7/2 and Pt4f5/2 in Pt (0) species.[35-36] Combined with H_2-TPR test results, it can be obtained that platinum atoms has been reduced completely. In addition, there are two distinct peaks in the 712.3 eV and 725.9 eV, corresponding to the binding energy of Fe2p3/2 and Fe2p1/2 in Fe^{3+} species. Compared with the Fe^{3+} species of ferric oxide, this value reveals a shift of 0.5-1 eV towards higher binding energy.[37] This result can be considered that most of the iron atoms were incorporated into the framework and form a stable Fe-O-Si bond.[38] The two weak characteristic peaks at 719 eV and 732 eV represent the shakeup satellites of Fe2p peaks.[39] At the same time, O1s spectra of all the samples only has one characteristic peak at 532.6 eV (Fig. S3 in ESI), which indicates that there is only one type of oxygen atom in the sample. It further illustrates that there almost has no any other form of oxides except for the framework oxygen.

3.2 Catalytic performance

The activity of the catalyst was tested by hydrocracking of residue oil. The effect of reaction conditions on the conversion of residue oil and selectivity of gasoline was investigated over 0.3%Pt@7%Fe-MCM-41 sample and the results are shown in Fig.8. Fig. 8A represents the influence of different reaction pressure on the activity of catalyst. The conversion of residue oil and gasoline selectivity increased gradually as the pressure increases, which is because the high pressure can increase the number of collisions and the contact area between reactants and catalysts. When the pressure exceeded 5.5MPa, the selectivity of gasoline decreased on the contrary. The reason is that higher pressure is conducive to produce more dry gas composition and lead to the relatively decrease of gasoline selectivity. Therefore, the most suitable pressure was selected as 5.5 MPa.

Fig. 8B shows the influence of different reaction temperature. The hydrocracking of residual oil belongs to endothermic reaction, so higher temperature is beneficial for this procedure. When the reaction temperature was 250 °C, the conversion of residual oil was only 51%. When the reaction temperature increased to 350 °C, the conversion of the residue oil reached 79.7%, and the selectivity of gasoline reached 62%. However, the catalytic activity remain unchanged as the temperature reached 400 °C. On the contrary, the coke yield appeared to increase, so the optimum reaction temperature is 350 °C. Fig. 8C is the influence of different WHSV. The conversion and selectivity of the catalytic cracking reaction are related to the contact time between reactants and catalysts.

When the WHSV is small, the residual oil and the catalysts can fully contact and react, and further can result in a higher conversion. When the WHSV was greater than 10 h^{-1}, the conversion of residue oil and selectivity of gasoline reduced because of the shot contact time. When the WHSV was lower than 10 h^{-1}, the gasoline selectivity decreased, which attribute to the excessive cracking of residual oil and producing more dry gas. Based on the above factors, the suitable WHSV was chosen as 10 h^{-1} without affecting the reactant conversion.
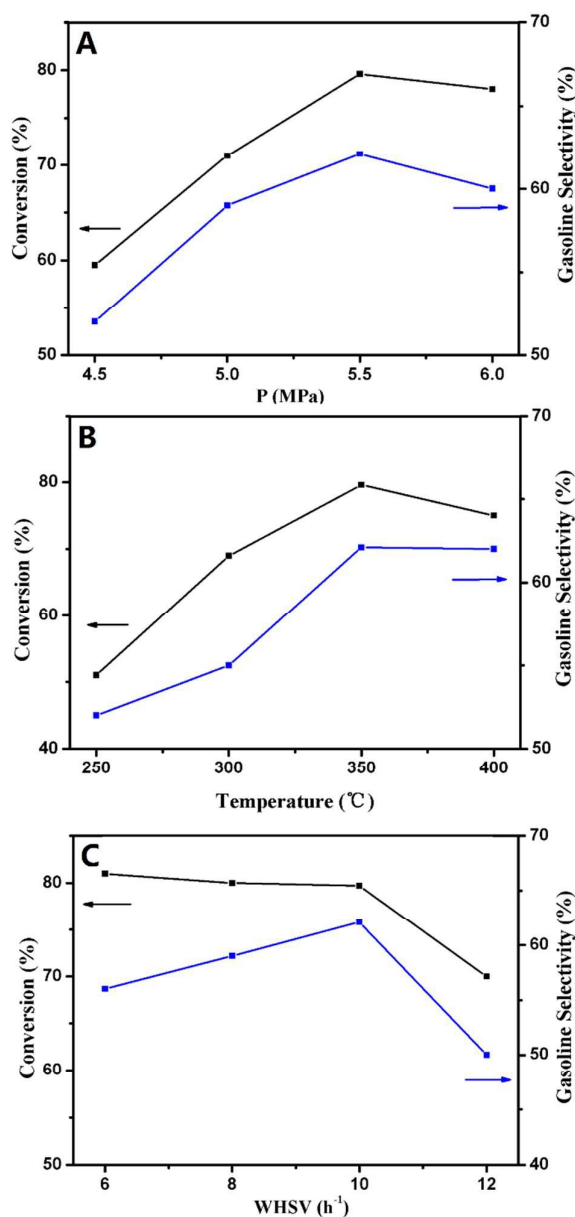
Fig. 8 The conversion of oil and the selectivity of gasoline under different reaction conditions: A. at different pressure, B. at different temperature, C. at different WHSV.

Table 2 Conversion and product selectivity of residual oil over different catalysts

samples	Conversion (%)	selectivity（%）				
		gas	Gasoline	Kerosene	Coke	others
0.3%Pt@7%Fe-MCM-41	79.7	1.7	62.1	29.6	3.7	2.9
0.3%Pt@10%Fe-MCM-41	84.5	2.1	69.7	21.2	4.1	2.9
0.3%Pt@12%Fe-MCM-41	87.8	2.8	74.3	15.2	5.0	2.7
0.3%Pt/12%Fe-MCM-41	73.0	2.3	59.7	28.5	5.7	3.8
12%Fe-MCM-41	62.8	2.9	49.5	29.8	11.3	6.5

Under the above conditions, the catalytic results over different catalysts are summarized in table 2. The conversion of the residue oil could reach 87.8% and the selectivity of gasoline could reach 74.3% over the 0.3%Pt@x%Fe-MCM-41 catalysts. Compared with a single metal modified catalyst, the catalytic activity of this novel bifunctional catalyst was improved observably. For the 12%Fe-MCM-41 sample, the conversion of residue oil and the selectivity of gasoline were 62.8% and 49.5% respectively. The weak hydrogenation ability of Fe is the primary reason for the poor catalytic activity. In addition, the 0.3%Pt/12%Fe-MCM-41 sample also show a relative weak activity because part of platinum nanoparticles accumulated in a random way on the external surface and aggregated to big block (Fig. S4, ESI). The above results prove that the highly dispersed platinum nanoparticles have a stronger promotion for the activity of Fe-MCM-41. The NH_3-TPD curves of different samples have been shown in Fig. S5 (ESI). Compared with the catalyst prepared by impregnation method, the novel bifunctional catalysts appear a strong and broad desorption peak at 200-400 ^{o}C, corresponding to the moderately strong acid center. And the peak area and strength of acid centers are increase with the Fe content obviously, which illustrate that Fe was incorporated into the framework of MCM-41 and increased the acid strength of the bifunctional catalysts. The XRD patterns of 0.3%Pt@7%Fe-MCM-41 sample before and after reaction are shown in Fig. S6 (ESI). It can be seen that even though there have obvious reduction and broadening of the diffraction peaks after hydrocracking reaction, the sample also maintain a relative regular structure. It proves that this novel bifunctional catalyst can tolerate the harsh reaction to a certain extent and will has practical applications in this area. During the whole process, when the reactants enter the pore structure, the highly dispersed metal active sites will rapidly carry out the hydrogenation reaction of unsaturated hydrocarbon and the product will immediately be cracked over the highly dispersed acid sites of the carrier. In the end, the small molecule products escape from the mesoporous channels in time and the highly dispersed metal compounds and acid centres will ensure a high efficient response for the reaction.

4. Conclusion

A new type of highly dispersed bifunctional catalyst Pt@Fe-MCM-41 was successfully prepared by in situ synthesis combined with selective reduction. In this catalyst, Fe^{3+} ions were highly dispersed in the framework of MCM-41 in the form of isomorphous substitution and platinum nanoparticles with the mean size of 2-3 nm were highly dispersed stably in the inner surface of the mesoporous channels, so that the catalyst has the highly dispersed acid catalytic sites and metal active sites simultaneously. The catalyst showed an excellent catalytic performance for hydrocracking of residual oil, and the highly dispersed metal and acid sites will ensure a high efficient response for the reaction.

Acknowledgements

Notes and references

1 C. Martínez and A. Corma, *Coordin. Chem. Rev.*, 2011, **255**, 1558.
2 S. Sartipi, M. Makkee, F. Kapteijn and J. Gascon, *Catal. Sci. Technol.*, 2014, **4**, 893.
3 K. Fan, J. Liu, X. Yang and L. Rong, *RSC Adv.*, 2015, **5**, 37916.
4 B. A. Alwan, S. O. Salley and K.Y. Simon Ng, *Appl. Catal. A: Gen.*, 2014, **485**, 58.
5 B. S. Li, J. Xu, X. Li, J Liu, S Zuo, Z Pan and Z Wu, *Mater. Res. Bull.*, 2012, **47**, 1142.
6 K. Fan, X. Yang, J. Liu and L. Rong, *RSC Adv.*, 2015, **5**, 33339.
7 X. Liu, L. Xu, B. Zhang and X. Liu, *Microporous Mesoporous Mater.*, 2014, **193**, 127.
8 R. Sahu, B. J. Song, J. S. Im, Y. Jeon and C. W. Lee, *J. Ind. Eng. Chem.*, 2015, **27**, 12.
9 W. Vermeiren and J. P. Gilson, *Top. Catal.* 2009, **52**, 1131.
10 A. Gutiérrez, J. M. Arandes, P. Castaño, M. Olazar, A. Barona and J. Bilbao, *Fuel Process. Technol.*, 2012, **95**, 8.
11 B. D. Vandegehuchte, J. W. Thybaut, A. Martínez, M. A. Arribas and G. B. Marin, *Appl. Catal. A: Gen.*, 2012, **441-442**, 10.

12 F. A. Khowatimy, Y. Priastomo, E. Febriyanti, H. Riyantoko and W. Trisunaryanti, *Procedia Environ. Sci.*, 2014, **20**, 225.
13 T. Hanaoka, T. Miyazawa, K. Shimura and S. Hirata, *Chem. Eng. J.*, 2015, **274**, 256.
14 A. Ishihara, N. Fukui, H. Nasu and T. Hashimoto, *Fuel*, 2014, **134**, 611.
15 C. T. Kresge, M. E. Leonowicz, W. J. Roth, J. C. Vartuli and J. S. Beck, *Nature*, 1992, **359**, 710.
16 J. S. Beck, J. C. Vartuli, W. J. Roth, M. E. Leonowicz, C. T. Kresge, K. D. Schmitt, C. T. W. Chu, D. H. Olson and E. W. Sheppard, *J. Am. Chem. Soc.*, 1992, **114**, 10834.
17 B. A. Alwan, S. O. Salley and K. Y..Simon Ng, *Appl. Catal. A: Gen.*, 2014, **485**, 58.
18 D. Rath and K. M. Parida, *Ind. Eng. Chem. Res.*, 2011, **50**, 2839.
19 M. Chatterjee, T. Ishizaka and H. Kawanami, *J. Colloid Interface Sci.*, 2014, **420**, 15.
20 A. Taguchi and F. Schüth, *Microporous Mesoporous Mater.*, 2005, **77**, 1.
21 J. Qin, B. Li, W. Zhang, W. Lv, C. Han and J. Liu, *Microporous Mesoporous Mater.*, 2015, **208**, 181.
22 A.M. Alsobaai, R. Zakaria and B.H. Hameed, *Chem. Eng. J.*, 2007, **132**, 173.
23 M. Seo, D. Lee, K. Lee and D. J. Moon, *Fuel*, 2015, **143**, 63.
24 A. E. Barrón C., J. A. Melo-Banda, J. M. Dominguez E., E. Hernández M., R. Silva R., A. I. Reyes T. and M. A. Meraz M., *Catal. Today*, 2011, **166**, 102.
25 B. S. Li, X. Li, J. Xu, X. Pang, X. Gao and Z. Zhou, *J. Colloid Interface Sci.*, 2010, **346**, 199.
26 J. Lin, B. Zhao, Y. Cao, H. Xu, S. Ma, M. Guo, D. Qiao and Y. Cao, *Appl. Catal. A: Gen.*, 2014, **478**, 175.
27 S. Samanta, S. Giri, P. U. Sastry, N. K. Mal, A. Manna and A. Bhaumik, *Ind. Eng. Chem. Res.*, 2003, **42**, 3012.
28 R. Fricke, H. Kosslick, G. Lischke and M. Richter, *Chem. Rev.*, 2000, **100**, 2303.
29 Q. Zhang, Y. Li, D. An and Y. Wang, *Appl. Catal. A: Gen.*, 2009, **356**, 103.
30 A. I. Carrillo, E. Serrano, R. Luque and J. García-Martínez, *Appl. Catal. A: Gen.*, 2013, **453**, 383.
31 A. Banisharif, A. A. Khodadadi, Y. Mortazavi, A. A. Firooz, J. Beheshtian, S. Agah and S. Menbari, *Appl. Catal. B: Environ.*, 2015, **165**, 209.
32 N. I. Cuello, V. R. Elías, C. E. Rodriguez Torres, M. E. Crivello, M. I. Oliva, G. A. Eimer, *Microporous Mesoporous Mater.,* 2015, **203**, 106.
33 B. S. Li, J. Xu, J. Liu, S. Zuo, Z. Pan and Z. Wu, *J. Colloid Interface Sci.*, 2012, **366**, 114.
34 L. F. Liotta, A. Longo, A. Macaluso, A. Martorana, G. Pantaleo, A. M. Venezia and G. Deganello, *Appl. Catal. B: Environ.*, 2004, **48**, 133.
35 H. Liu, G. Lu, Y. Guo, Y. Wang and Y. Guo, *J. Colloid Interface Sci.*, 2010, **346**, 486.
36 L. Li, P. Wu, Q. Yu, G. Wu and N. Guan, *Appl. Catal. B: Environ.*, 2010, **94**, 254.
37 T. C. Lin, G. Seshadri and J. A. Kelber, *Appl. Surf. Sci.*, 1997, **119**, 83.
38 A. De Stefanis, S. Kaciulis and L. Pandolfi, *Microporous Mesoporous Mater.*, 2007, **99**, 140.
39 T. Yamashita and P. Hayes, *Appl. Surf. Sci.*, 2008, **254**, 2441.

Graphical abstract
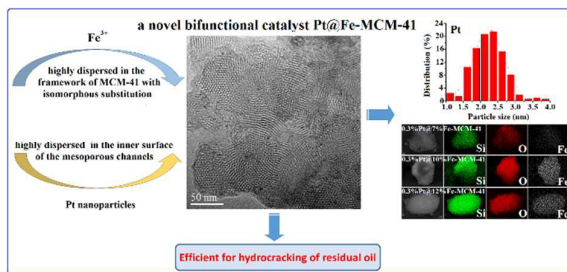
A novel bifunctional catalyst Pt@Fe-MCM-41 containing highly dispersed metal and acid active sites was synthesized successfully with excellent catalytic performance.